A&A, 708, A68 (2026)
https://doi.org/10.1051/0004-6361/202659417

Astronomy & Astrophysics

Alfvén wave propagation in the partially ionized lower solar atmosphere: A test of the single-fluid approximation

Roberto Soler[1,2,⋆]

[1] Departament de Física, Universitat de les Illes Balears, 07122 Palma de Mallorca, Spain
[2] Institut d'Aplicacions Computacionals de Codi Comunitari (IAC3), Universitat de les Illes Balears, 07122 Palma de Mallorca, Spain

Received 11 February 2026 / Accepted 4 March 2026

ABSTRACT

Alfvén waves are widely believed to play an important role in the transport of energy from the solar photosphere to the corona through the partially ionized chromosphere. In previous work, the properties of torsional Alfvén waves were theoretically studied using a multi-fluid model. Here, we compare those multi-fluid results with results obtained using the single-fluid magnetohydrodynamic approximation, as a way to assess the performance of the latter in the context of Alfvénic waves in the lower solar atmosphere. We considered a broadband photospheric driver that excites torsional Alfvén waves with frequencies ranging from 0.1 mHz to 300 mHz. These waves propagate upward to the corona along a magnetic flux tube that expands with height. We compared the energy flux, chromospheric reflection, transmission and absorption coefficients, and associated heating rates yielded by the two models. In general, the results of the two models are almost identical, with two minor differences: (1) the net energy flux that reaches the corona is approximately 5% higher in the single-fluid model, mainly owing to the higher reflectivity found in the multi-fluid model for wave frequencies exceeding 10 mHz; and (2) in a narrow region around 500 km above the photosphere, the single-fluid model underestimates the plasma heating rate due to ion-neutral damping by about a factor of two compared with the multi-fluid model. Both discrepancies arise from the approximate treatment of the ion-neutral drift in the single-fluid model and are expected to have a very limited impact in practical applications.

Key words. magnetohydrodynamics (MHD) – waves – Sun: chromosphere – Sun: corona – Sun: oscillations

1. Introduction

Alfvén waves are a type of incompressible magnetohydrodynamic (MHD) wave whose excitation in the solar atmosphere by photospheric granulation was postulated by Alfvén himself (Alfvén 1947). In cylindrically symmetric magnetic flux tubes, pure Alfvén modes[1] correspond to torsional waves, which produce axisymmetric velocity and magnetic field perturbations polarized in the azimuthal direction (see, e.g., Erdélyi & Fedun 2007). There is observational evidence of torsional Alfvén waves propagating through various layers of the solar atmosphere: the photosphere (Jess et al. 2009), the chromosphere and transition region (De Pontieu et al. 2012, 2014), and the corona (Morton et al. 2026). It has been theoretically shown that these waves can partially overcome the strong filtering caused by chromospheric reflection and dissipation, and thus provide a significant energy input to the coronal medium (see, e.g., Soler et al. 2017, 2019). In coronal flux tubes, these torsional waves can nonlinearly generate turbulence (see, e.g., Guo et al. 2019; Díaz-Suárez & Soler 2021).

The solar chromosphere is a partially ionized region (see, e.g., Martínez-Sykora et al. 2015), and it is well known that partial ionization of the plasma strongly affects the properties of MHD waves (see the review by Soler 2024). The theoretical study of MHD waves in partially ionized solar plasma is usually carried out using two approaches: single-fluid and multi-fluid models (see Khomenko et al. 2014; Ballester et al. 2018). The single-fluid approximation assumes that all species (in particular, ions and neutrals) are strongly coupled, and the effects of their interaction appear as nonideal terms in the governing equations. Among these nonideal terms, ambipolar diffusion plays a predominant role. Some representative wave studies in the solar context that use the single-fluid approximation include Khodachenko et al. (2004), Leake et al. (2005), Forteza et al. (2007), Goodman (2011), Arber et al. (2016), and Cally & Khomenko (2019). Conversely, in the multi-fluid description, the degree of coupling between different species is allowed to be arbitrary, and interaction terms are explicitly included in the equations. A particular version of the multi-fluid description is the two-fluid model, in which charged particles and neutrals form two separate fluids. Examples of wave studies using the multi-fluid approach include Zaqarashvili et al. (2011), Song & Vasyliūnas (2011), Tu & Song (2013), Maneva et al. (2017), Martínez-Gómez et al. (2017, 2018), Popescu Braileanu et al. (2019), Pelekhata et al. (2021), and Cally (2023), among many others.

The multi-fluid model provides a more accurate physical description than the single-fluid approximation, though its use in analytical studies and its implementation in numerical codes are both more involved. Nevertheless, owing to the high values of collision frequencies in the lower solar atmosphere (see Ballester et al. 2018), the single-fluid approximation often yields a sufficiently accurate description, although its accuracy can depend on the specific process under investigation. The purpose of this paper is to revisit the study of torsional Alfvén wave

⋆ Corresponding author: roberto.soler@uib.es

[1] By pure Alfvén modes we mean Alfvén waves that are not coupled with another type of mode.

propagation from the photosphere to the corona presented in Soler et al. (2019), who employed a multi-fluid model. Here, we aim to compare the Soler et al. (2019) multi-fluid results with those obtained using the single-fluid model as a means of assessing the performance of the single-fluid approximation in the context of Alfvén waves in the partially ionized lower solar atmosphere. Recently, Gómez-Míguez et al. (2025) carried out an investigation with a similar goal, though their study and the present work differ in several aspects, such as the background configuration, methodology, and the type of wave studied.

This paper is organized as follows. Section 2 describes the model, the governing equations, and the methodology. Section 3 presents a comparison of the multi-fluid and single-fluid results. Finally, Sect. 4 provides a discussion and concluding remarks.

2. Model, basic equations, and method

2.1. Background atmosphere

The background atmosphere and magnetic field model are the same as those used in Soler et al. (2019). We refer readers to the previous paper for detailed explanations; here, we provide only a brief summary.

The atmosphere is a gravitationally stratified medium whose physical properties vary with height according to an adapted version of the quiet-Sun chromospheric model C of Fontenla et al. (1993). The atmosphere is plane-parallel, so the plasma properties are invariant in the horizontal directions. The model extends from the base of the photosphere through the chromosphere and the transition region, reaching the low corona at 4000 km above the photosphere. The plasma is composed of hydrogen and helium and is partially ionized. A strong thermal coupling is assumed between all species, so they share a common temperature. The variation of the total density and temperature with height according to this model can be seen in Fig. 1 of Soler et al. (2019).

The magnetic field configuration consists of a potential flux tube that expands with height from the photosphere to the corona. The tube axis is vertical, and the field lines are untwisted. We used cylindrical coordinates with the z-axis directed along the flux tube axis, which coincides with the vertical direction. Hence, the background magnetic field vector, $\mathbf{B}$, is expressed as

$$\mathbf{B} = B_r(r,z)\,\hat{e}_r + B_z(r,z)\,\hat{e}_z. \tag{1}$$

The magnetic flux tube is numerically constructed by imposing that $\mathbf{B}$ satisfies both the current-free ($\nabla \times \mathbf{B} = 0$) and divergence-free ($\nabla \cdot \mathbf{B} = 0$) conditions. At the photosphere, the tube radius is set to 100 km, with a magnetic field strength at the tube center of 1 kG. The radius increases with height due to tube expansion, reaching 1000 km in the low corona. Because of conservation of magnetic flux, the magnetic field strength decreases with height, reaching a minimum of 10 G in the low corona, where the field becomes purely vertical. A three-dimensional visualization of the flux tube embedded in the stratified atmosphere can be seen in Fig. 1.

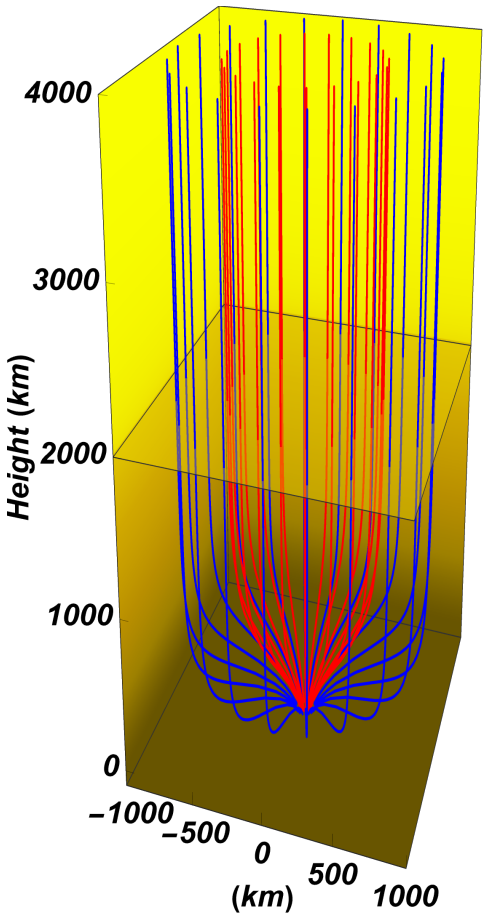

Fig. 1. Equilibrium magnetic flux tube model embedded in the background atmosphere. The red and blue lines outline some selected magnetic field lines that cross the photosphere at 40 km and 70 km from the tube axis, respectively. The color gradient illustrates the density stratification from the photosphere (brown) to the low corona (yellow). The transition region height is marked by a horizontal, semitransparent plane. For visualization purposes, the horizontal and vertical directions are not to scale.

2.2. From multi-fluid equations to the single-fluid approximation

The propagation of linear torsional Alfvén waves from the photosphere to the corona in the model described above was investigated in Soler et al. (2019) using a multi-fluid treatment. All ions (protons, singly ionized helium, and doubly ionized helium) were treated together as a single ionic fluid, while neutral hydrogen and neutral helium were treated as two separate neutral fluids. The three fluids exchanged momentum through particle collisions. Electron inertia was neglected, while collisions of electrons with the other species gave rise to the magnetic diffusion (i.e., resistivity) term in the induction equation.

Here, the goal is to use the single-fluid approximation to further reduce the number of independent fluids considered in the plasma treatment. To this end, we closely followed the derivation given in Zaqarashvili et al. (2013). Readers are also referred to Khomenko et al. (2014), Ballester et al. (2018), and references therein for more details on the physical and mathematical subtleties of this approach.

We started from the linearized equations of motion and the linearized induction equation used in Soler et al. (2019), namely

$$\rho_{\rm i}\frac{\partial \mathbf{v}'_{\rm i}}{\partial t} = \frac{1}{\mu}(\nabla \times \mathbf{B}') \times \mathbf{B} - \alpha_{\rm iH}\left(\mathbf{v}'_{\rm i} - \mathbf{v}'_{\rm H}\right) - \alpha_{\rm iHe}\left(\mathbf{v}'_{\rm i} - \mathbf{v}'_{\rm He}\right), \tag{2}$$

$$\rho_{\rm H}\frac{\partial \mathbf{v}'_{\rm H}}{\partial t} = -\alpha_{\rm Hi}\left(\mathbf{v}'_{\rm H} - \mathbf{v}'_{\rm i}\right) - \alpha_{\rm HHe}\left(\mathbf{v}'_{\rm H} - \mathbf{v}'_{\rm He}\right), \tag{3}$$

$$\rho_{\rm He}\frac{\partial \mathbf{v}'_{\rm He}}{\partial t} = -\alpha_{\rm He\,i}\left(\mathbf{v}'_{\rm He}-\mathbf{v}'_{\rm i}\right)-\alpha_{\rm He\,H}\left(\mathbf{v}'_{\rm He}-\mathbf{v}'_{\rm H}\right), \quad (4)$$

$$\frac{\partial \mathbf{B}'}{\partial t} = \nabla\times\left(\mathbf{v}'_{\rm i}\times\mathbf{B}\right)-\nabla\times\left[\eta\left(\nabla\times\mathbf{B}'\right)\right]. \quad (5)$$

In these equations, subscripts i, H, and He denote the ions, neutral hydrogen, and neutral helium, respectively. We use subscript β to refer to an arbitrary species such that ρ_β and $\mathbf{v}'_\beta$ are the mass density and velocity perturbation of species β, respectively. In turn, $\mathbf{B}$ and $\mathbf{B}'$ are the background magnetic field (defined before) and the magnetic field perturbation, respectively. Finally, $\alpha_{\beta\beta'} = \alpha_{\beta'\beta}$ is the symmetric friction coefficient for collisions between species β and β', and η is the coefficient of resistivity or Ohmic diffusion. The expressions of these various coefficients are given Soler et al. (2019) but are omitted here for the sake of simplicity. The dependence of η on height in the atmospheric model is shown in the bottom panel of Fig. 2. We note that gas pressure terms are omitted from these equations because they are irrelevant for the investigation of Alfvén waves.

The process of deriving the single-fluid equations begins by defining the total density, ρ, and the center-of-mass velocity perturbation, $\mathbf{v}'$, as

$$\rho \equiv \rho_{\rm i}+\rho_{\rm H}+\rho_{\rm He}, \quad (6)$$

$$\mathbf{v}' \equiv \xi_{\rm i}\mathbf{v}'_{\rm i}+\xi_{\rm H}\mathbf{v}'_{\rm H}+\xi_{\rm He}\mathbf{v}'_{\rm He}, \quad (7)$$

where $\xi_\beta = \rho_\beta/\rho$ is the fraction of species β. To obtain approximate expressions for the ion-neutral velocity drifts, we performed consecutive subtractions of the various momentum equations and neglected the differences of the inertia terms (see details in Zaqarashvili et al. 2013). The velocity drifts are found to be proportional to the Lorentz force and can be cast as

$$\mathbf{v}'_{\rm i}-\mathbf{v}'_{\rm H} \approx C_{\rm H}\frac{1}{\mu}\left(\nabla\times\mathbf{B}'\right)\times\mathbf{B}, \quad (8)$$

$$\mathbf{v}'_{\rm i}-\mathbf{v}'_{\rm He} \approx C_{\rm He}\frac{1}{\mu}\left(\nabla\times\mathbf{B}'\right)\times\mathbf{B}, \quad (9)$$

with the proportionality factors given by

$$C_{\rm H} = \frac{\xi_{\rm H}\alpha_{\rm i\,He}+\left(\xi_{\rm H}+\xi_{\rm He}\right)\alpha_{\rm H\,He}}{\alpha_{\rm i\,H}\alpha_{\rm i\,He}+\left(\alpha_{\rm i\,H}+\alpha_{\rm i\,He}\right)\alpha_{\rm H\,He}}, \quad (10)$$

$$C_{\rm He} = \frac{\xi_{\rm He}\alpha_{\rm i\,H}+\left(\xi_{\rm H}+\xi_{\rm He}\right)\alpha_{\rm H\,He}}{\alpha_{\rm i\,H}\alpha_{\rm i\,He}+\left(\alpha_{\rm i\,H}+\alpha_{\rm i\,He}\right)\alpha_{\rm H\,He}}. \quad (11)$$

The validity of the approximate Eqs. (8) and (9) relies on the conditions that the wave frequency is much lower than the collision frequencies between ions and neutrals and that the magnitude of the velocity drifts are much smaller than the thermal velocity[2]. The frequency of collisions between species β and β' is

$$\nu_{\beta\beta'} = \frac{\alpha_{\beta\beta'}}{\rho_\beta}. \quad (12)$$

The top panel of Fig. 2 shows the height dependence of the collision frequencies involving neutrals in the atmospheric model. We note that all these frequencies vanish above the transition region, where the plasma becomes fully ionized. The most restrictive frequency is that of collisions between neutral helium and ions, $\nu_{\rm He\,i}$, whose minimum value is approximately 2 Hz at 500 km above the photosphere. Therefore, waves with lower frequencies should satisfy the conditions for the applicability of the single-fluid approximation. We note that if the plasma were composed only of hydrogen, the most restrictive frequency would be that of collisions between neutral hydrogen and ions, $\nu_{\rm H\,i}$, which is approximately an order of magnitude higher than $\nu_{\rm He\,i}$ at those heights. The presence of helium reduces the range of applicability of the single-fluid approximation to lower frequencies.

[2] A more general formulation has been discussed by Hillier (2024).

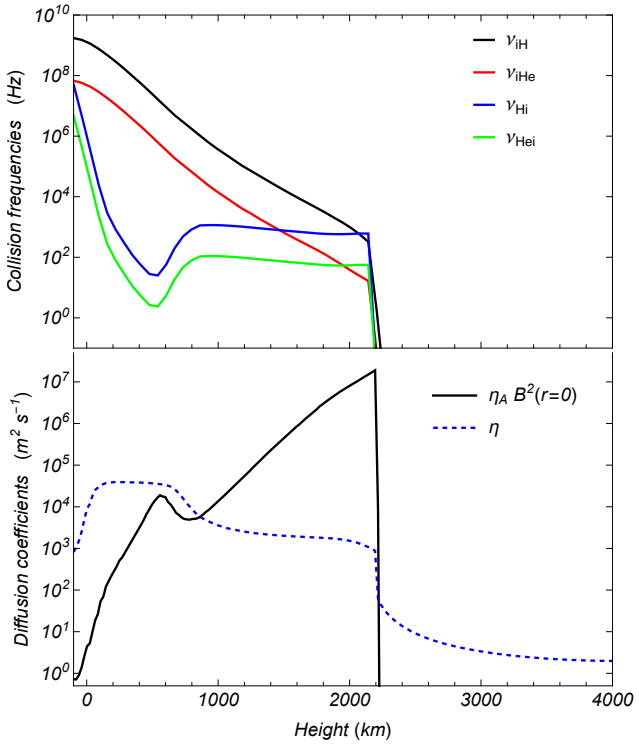

Fig. 2. Dependence on height above the photosphere of the collision frequencies involving neutrals (top) and the Ohmic and ambipolar diffusion coefficients (bottom) according to the assumed background atmospheric model. The ambipolar coefficient was computed using the magnetic field strength at the axis of the flux tube.

The relation between the ion-neutral drift associated with hydrogen and that associated with helium can be estimated by taking the ratio of Eqs. (8) and (9), namely

$$\frac{\mathbf{v}'_{\rm i}-\mathbf{v}'_{\rm H}}{\mathbf{v}'_{\rm i}-\mathbf{v}'_{\rm He}} \approx \frac{\nu_{\rm He\,i}}{\nu_{\rm H\,i}}, \quad (13)$$

where, for simplicity, collisions between the two neutral species have been neglected in this comparison. Since $\nu_{\rm He\,i} < \nu_{\rm H\,i}$ throughout the chromosphere, the ion-neutral drift associated with helium is expected to be larger than that associated with hydrogen.

By combining Eqs. (8) and (9) with Eq. (7), we can approximate the ion velocity perturbation as

$$\mathbf{v}'_{\rm i} \approx \mathbf{v}' + \eta_{\rm A}\left(\nabla\times\mathbf{B}'\right)\times\mathbf{B}, \quad (14)$$

where the second term on the right-hand side represents the ambipolar drift, with $\eta_{\rm A}$ being the ambipolar coefficient, given by

$$\eta_{\rm A} = \frac{\xi_{\rm H}C_{\rm H}+\xi_{\rm He}C_{\rm He}}{\mu}. \quad (15)$$

Using the expressions for $C_{\rm H}$ and $C_{\rm He}$ from Eqs. (10) and (11), and after some algebra, the ambipolar coefficient can be

rewritten as

$$\eta_{\rm A} = \frac{\xi_{\rm H}^2\alpha_{\rm He} + \xi_{\rm He}^2\alpha_{\rm H} + 2\xi_{\rm H}\xi_{\rm He}\alpha_{\rm H\,He}}{\mu\left(\alpha_{\rm H}\alpha_{\rm He} - \alpha_{\rm H\,He}^2\right)}, \tag{16}$$

where $\alpha_\beta = \sum_{\beta'\neq\beta}\alpha_{\beta\beta'}$ is the total friction coefficient of species β. Equation (16) agrees with the expression of $\eta_{\rm A}$ for a hydrogen-helium plasma previously obtained by Zaqarashvili et al. (2013).

A comparison of the values of η and $\eta_{\rm A}$ in the atmospheric model is shown in the bottom panel of Fig. 2. We note that the SI units of $\eta_{\rm A}$ are $\mathrm{m^2\,s^{-1}\,T^{-2}}$, so the quantity that actually corresponds to a diffusion coefficient is $\eta_{\rm A}|\mathbf{B}|^2$. Therefore, the efficiency of ambipolar diffusion depends on the magnetic field strength. Assuming a magnetic field strength equal to that at the center of the flux tube, we find that ambipolar diffusion dominates over Ohmic diffusion from approximately 1000 km above the photosphere up to the transition region, where the plasma becomes fully ionized. A similar plot can be seen in Fig. 1 of Khomenko & Collados (2012), although for a different magnetic field configuration.

The single-fluid version of the linearized momentum equation is obtained by simply adding Eqs. (2), (3), and (4) such that the collisional terms cancel out, giving

$$\rho\frac{\partial\mathbf{v}'}{\partial t} = \frac{1}{\mu}\left(\nabla\times\mathbf{B}'\right)\times\mathbf{B}. \tag{17}$$

For the linearized induction Equation (Eq. (5)), we use Eq. (14) to express the ion velocity perturbation in terms of the center-of-mass velocity and the ambipolar drift. By doing so, a term accounting explicitly for ambipolar diffusion appears in the induction equation:

$$\begin{aligned}\frac{\partial\mathbf{B}'}{\partial t} &= \nabla\times(\mathbf{v}'\times\mathbf{B}) - \nabla\times\left[\eta\left(\nabla\times\mathbf{B}'\right)\right]\\ &\quad + \nabla\times\left\{\eta_{\rm A}\left[\left(\nabla\times\mathbf{B}'\right)\times\mathbf{B}\right]\times\mathbf{B}\right\},\end{aligned} \tag{18}$$

where the ambipolar term is the third term on the right-hand side.

In summary, Eqs. (17) and (18) form the basic linearized equations for discussing Alfvén waves in the single-fluid approximation. As in the initial multi-fluid Eqs. (2)–(5), gas pressure terms are omitted. Since we have already considered linearized equations at the beginning of the derivation, Eqs. (17) and (18) are not generally applicable beyond the context of linear Alfvén waves, but they suffice for our present goals. The complete nonlinear single-fluid equations can be found in, e.g., Khomenko et al. (2014) and Ballester et al. (2018).

2.3. Governing equations for torsional Alfvén waves

From here on, we focus on purely torsional Alfvén waves. We used cylindrical coordinates and assumed that the only nonzero perturbations are the azimuthal components of $\mathbf{v}'$ and $\mathbf{B}'$, namely

$$\mathbf{v}' = v'_\varphi\hat{e}_\varphi, \qquad \mathbf{B}' = B'_\varphi\hat{e}_\varphi. \tag{19}$$

Furthermore, we considered the stationary state of wave propagation[3]. We express the temporal dependence of v'_φ and B'_φ as $\exp(-i\omega t)$, where ω is the angular frequency of the waves. Thus, from Eq. (17) we can write v'_φ in terms of B'_φ as

$$v'_\varphi = \frac{i}{\omega}\frac{1}{\mu\rho}\frac{1}{r}\mathbf{B}\cdot\nabla\left(rB'_\varphi\right). \tag{20}$$

[3] The validity of this approach has been assessed in Soler (2025) against the full temporal evolution.

Using Eq. (20) in Eq. (18) to replace v'_φ, we obtain a partial differential equation involving B'_φ alone:

$$\begin{aligned}&i\omega B'_\varphi + r\mathbf{B}\cdot\nabla\left[\frac{i}{\omega}\frac{1}{\mu\rho}\frac{1}{r^2}\mathbf{B}\cdot\nabla\left(rB'_\varphi\right)\right] + \eta\left(\nabla^2B'_\varphi - \frac{1}{r^2}B'_\varphi\right)\\ &\quad + \frac{\partial\eta}{\partial z}\frac{\partial B'_\varphi}{\partial z} + \eta_{\rm A}\left\{\mathbf{B}\cdot\nabla\left[\frac{1}{r}\mathbf{B}\cdot\nabla\left(rB'_\varphi\right)\right] - \frac{B_r}{r^2}\mathbf{B}\cdot\nabla\left(rB'_\varphi\right)\right\}\\ &\quad + \frac{\partial\eta_{\rm A}}{\partial z}\frac{B_z}{r}\mathbf{B}\cdot\nabla\left(rB'_\varphi\right) = 0.\end{aligned} \tag{21}$$

Equation (21) is our main equation. It corresponds to the single-fluid version of Eq. (36) of Soler et al. (2019), which was derived in the multi-fluid case. Two differences arise between the single-fluid and multi-fluid equations, which are related to the different treatment of the ion-neutral (ambipolar) drift. In the present form of Eq. (21), there are terms proportional to $\eta_{\rm A}$ and $\partial\eta_{\rm A}/\partial z$, which explicitly account for the ambipolar drift as a diffusion mechanism for the magnetic field in the single-fluid approximation. Conversely, in the multi-fluid version of the equation, the effect of the ion-neutral drift is more subtly included in the second term through the effective density, $\rho_{\rm eff}$, which accounts for the fact that the inertia of the plasma in response to magnetic field oscillations depends on the strength of the coupling between ions and neutrals. The effective density is defined in Eq. (34) of Soler et al. (2019) and reduces to the total density, ρ, in the single-fluid limit, where all species are assumed to be strongly coupled. Thus, the second term in Eq. (21) consistently involves ρ instead of $\rho_{\rm eff}$ as in the multi-fluid version.

Using Eqs. (17) and (18), we derived an equation for the evolution of the wave energy following the method of Walker (2005). To retain the net energy contribution, we averaged the energy equation in time over a full period of the waves. The resulting time-averaged energy equation is

$$\frac{\partial\langle U\rangle}{\partial t} + \nabla\cdot\langle\mathbf{\Pi}\rangle = -\langle H\rangle, \tag{22}$$

where $\langle U\rangle$ is the time-averaged total energy density, $\langle\mathbf{\Pi}\rangle$ is the time-averaged energy flux, and $\langle H\rangle$ is the time-averaged dissipated energy, which represents a heating input for the background plasma. The expressions for these quantities are

$$\langle U\rangle = \frac{1}{4}\rho v'_\varphi v'^{\,*}_\varphi + \frac{1}{4\mu}B'_\varphi B'^{\,*}_\varphi, \tag{23}$$

$$\begin{aligned}\langle\mathbf{\Pi}\rangle &= -\frac{1}{2\mu}\mathrm{Re}\left(v'_\varphi B'^{\,*}_\varphi\right)\mathbf{B} - \frac{\eta_{\rm A}}{2\mu}\frac{1}{r}\mathbf{B}\cdot\nabla\left(rB'_\varphi\right)B'^{\,*}_\varphi\mathbf{B}\\ &\quad - \frac{\eta}{2\mu}\left(\frac{1}{r}\frac{\partial\left(rB'_\varphi\right)}{\partial r}B'^{\,*}_\varphi\hat{e}_r + \frac{\partial B'_\varphi}{\partial z}B'^{\,*}_\varphi\hat{e}_z\right),\end{aligned} \tag{24}$$

$$\begin{aligned}\langle H\rangle &= \frac{\eta}{2\mu}\left(\frac{1}{r^2}\frac{\partial\left(rB'_\varphi\right)}{\partial r}\frac{\partial\left(rB'^{\,*}_\varphi\right)}{\partial r} + \frac{\partial B'_\varphi}{\partial z}\frac{\partial B'^{\,*}_\varphi}{\partial z}\right)\\ &\quad + \frac{\eta_{\rm A}}{2\mu}\frac{1}{r^2}\mathbf{B}\cdot\nabla\left(rB'_\varphi\right)\mathbf{B}\cdot\nabla\left(rB'^{\,*}_\varphi\right),\end{aligned} \tag{25}$$

where $*$ denotes the complex conjugate.

The expression for the energy flux (Eq. (24)) contains three terms. The first term corresponds to the ideal Alfvén wave energy flux and is aligned exclusively along the direction of the background magnetic field. The second and third terms are corrections due to ambipolar diffusion (second term) and Ohmic diffusion (third term). The ambipolar-related term is also aligned with the background magnetic field, whereas the Ohmic-related

term has a component perpendicular to the background field. Nevertheless, this perpendicular component is orders of magnitude smaller than the field-aligned component (see Soler et al. 2019).

The energy flux in the multi-fluid case corresponds to Eq. (39) of Soler et al. (2019). An explicit ambipolar-related term is absent from the multi-fluid expression, but the ideal term is written in terms of the ion velocity perturbation instead of the center-of-mass velocity. This means that the effect of ambipolar diffusion on the energy flux is indeed included in the multi-fluid formalism, although not as an explicit term. Conversely, the Ohmic-related term is also present in Eq. (39) of Soler et al. (2019), but it was neglected in their computations. Here, we retain the Ohmic-related term and will demonstrate that its contribution is indeed negligible.

Concerning the expression for the heating rate (Eq. (25)), the term proportional to η corresponds to Ohmic heating, and the term proportional to η_A corresponds to ambipolar heating. In the single-fluid approximation, the ambipolar heating term replaces the frictional heating term that naturally appears in the multi-fluid formalism (see Eqs. (40)–(42) of Soler et al. 2019).

2.4. Numerical method

We adapted the numerical method described in Sect. 4 of Soler et al. (2019) to solve our main equation (Eq. (21)) using a finite-element-based code. The computational domain roughly corresponds to that shown in Fig. 1, although the code only solves in the radial and vertical directions due to the azimuthal invariance of torsional waves. A nonuniform mesh was employed to accurately capture the relevant spatial scales. Convergence tests have been carried out to determine the physically adequate spatial resolution. In the present context, the spatial resolution needs to correctly resolve the wavelength of the Alfvénic perturbations along the magnetic field direction and the small transverse scales developed by phase mixing. A very fine resolution of approximately 100 m is used in the photosphere and lower chromosphere, while the resolution decreases with height, reaching roughly 10 km in the low corona. This resolution is sufficient even for the highest wave frequencies considered here.

A driver for the torsional waves is assumed at the photosphere. Its effect is incorporated through the boundary condition at the lower boundary, where we imposed a twist of the magnetic field lines that excites torsional waves with frequencies between 0.1 mHz and 300 mHz. The adopted frequency range is motivated by observations of horizontal motions in the photosphere (see Matsumoto & Shibata 2010; Matsumoto & Kitai 2010; Chitta et al. 2012). Figure 2 of Matsumoto & Shibata (2010) shows that the power spectrum of photospheric horizontal velocity spans approximately from 0.16 mHz to 80 mHz, while the spectrum displayed in Fig. 3 of Matsumoto & Kitai (2010) roughly ranges between 0.2 mHz and 20 mHz. In turn, Fig. 9 of Chitta et al. (2012) covers a range from 0.1 mHz to 100 mHz. Here, the spectrum has been extended up to 300 mHz in order to account for higher frequencies that may not have been detected due to observational limitations. The spectral weighting function is inspired by those used in Tu & Song (2013) and Arber et al. (2016), and follows the same power-law form as described in Eq. (66) of Soler et al. (2019). The spectrum is discretized into 84 logarithmically spaced frequencies, with a random phase added to each discrete frequency to construct the full spectrum. The driver amplitude is adjusted so that the horizontally averaged injected wave energy flux is 10^7 erg cm^{-2} s^{-1}.

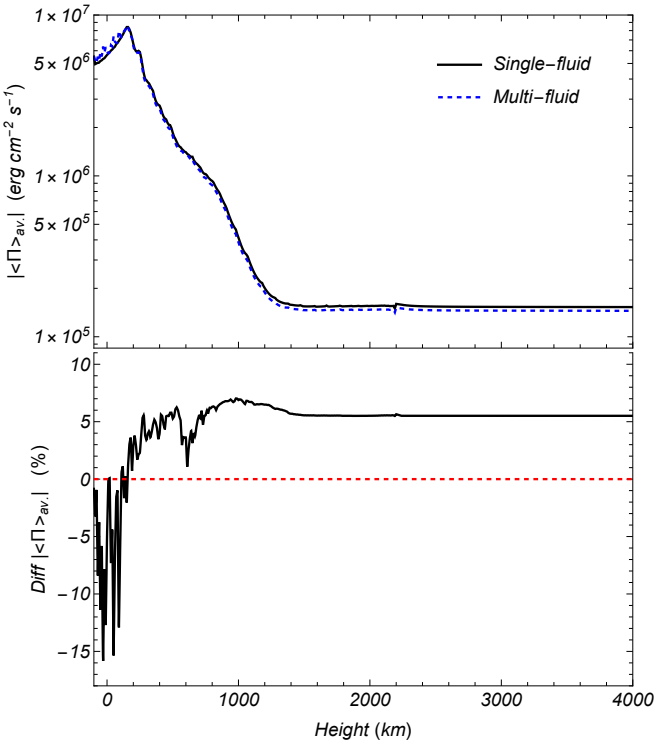

Fig. 3. Dependence on height above the photosphere of the horizontally averaged net energy flux in the single-fluid and multi-fluid models (top) and percentage difference of the single-fluid flux with respect to the multi-fluid flux (bottom).

In contrast to the lower boundary, the upper boundary is treated as perfectly transparent (i.e., nonreflective), allowing all waves that reach it to freely leave the domain. The boundary condition at the lateral edge of the domain, located at $r = r_{max} = 1000$ km, is that B'_φ vanishes.

3. Comparing single-fluid and multi-fluid results

We compared the results of the single-fluid model with those of the multi-fluid model. The multi-fluid results were taken from Soler et al. (2019) without modification. In contrast, the single-fluid results are new and were specifically computed for this paper. The main equation (Eq. (21)) is solved for each individual frequency in the spectrum. Then, the time-averaged terms in the wave energy equation (Eqs. (23)–(25)) are computed and, subsequently, the results for all the frequencies are added together according to the prescribed spectral weighting function.

First, we are interested in comparing the propagation of wave energy along the vertical direction, z. Therefore, to eliminate the dependence on the other two coordinates, r and φ, we horizontally averaged the energy flux over an area extending from $r = 0$ to $r = r_{max}$ as

$$\langle \mathbf{\Pi} \rangle_{av.} = \frac{1}{\pi r_{max}^2} \int_0^{2\pi} \int_0^{r_{max}} \langle \mathbf{\Pi} \rangle \, r \, dr \, d\varphi. \tag{26}$$

The horizontally averaged flux is a function of height alone. The top panel of Fig. 3 displays the horizontally averaged fluxes obtained in the two models. At the scale of the figure, the two results are nearly identical. The net energy flux decreases by several orders of magnitude with height, with only about 1% of the photospherically injected flux reaching the corona.

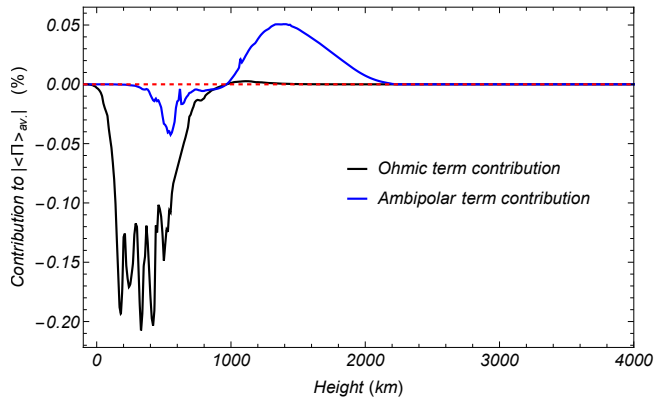

Fig. 4. Percentage contributions of the Ohmic term and the ambipolar term to the horizontally averaged net energy flux as functions of height above the photosphere. The horizontal dashed red line denotes no contribution. We show results of the single-fluid model.

As shown in Soler et al. (2019), this strong decrease is caused by two mechanisms: reflection and dissipation. Low-frequency waves are mainly reflected back toward the photosphere, with most of the reflection occurring in the middle and upper chromosphere, between about 1000 km above the photosphere and the transition region. High-frequency waves, instead, are efficiently dissipated. Dissipation operates in the lower chromosphere primarily via Ohmic diffusion, and in the middle chromosphere via ion–neutral collisions (or ambipolar diffusion in the single-fluid formalism).

An additional feature is a slight increase in the net flux in the very low chromosphere, up to ∼200 km above the photosphere, before the overall decrease sets in. This seemingly counterintuitive behavior arises from the horizontal averaging. While the average injected flux at the photosphere is 10^7 erg cm^{-2} s^{-1}, the small photospheric radius of the tube implies a much larger flux within the tube (∼10^9 erg cm^{-2} s^{-1}). Over the first 200 km, reflection and dissipation are still weak, so the upward flux inside the tube remains nearly constant, while the tube radius increases with height due to the expansion. As a result, the horizontally averaged flux increases transiently.

To highlight the differences between the two models, the bottom panel of Fig. 3 shows the percentage difference between the single-fluid and multi-fluid energy fluxes. In a narrow region near the photosphere, the single-fluid flux is up to 15% lower than the multi-fluid flux. At greater heights, this result reverses, and the single-fluid flux becomes slightly larger. At coronal heights, it exceeds the multi-fluid flux by approximately 5%, which implies that slightly more wave energy reaches the corona in the single-fluid model.

The nonideal terms were neglected in the computation of the energy flux in the multi-fluid model presented in Soler et al. (2019), but are included in the single-fluid computation. This raises the question of whether the differences between the single-fluid and multi-fluid energy fluxes could be attributed to these terms. To investigate this possibility, Fig. 4 displays the percentage contributions of the ambipolar and Ohmic terms relative to the ideal energy flux in the single-fluid model. These nonideal contributions correspond, respectively, to the second and third terms on the right-hand side of Eq. (24). The contributions of both terms turn out to be negligible, as assumed by Soler et al. (2019). Specifically, the ambipolar term has a negative contribution of about 0.2% in the low chromosphere, which seems insufficient to explain the discrepancy between the single-fluid and multi-fluid fluxes at low heights. The Ohmic term has a positive contribution of about 0.05% in the upper chromosphere, which is again negligible. Importantly, neither term contributes to the energy flux at coronal heights, which clearly indicates that the 5% excess of energy in the single-fluid model is not related to these terms.

To understand why slightly more energy reaches the corona in the single-fluid model, it is instructive to compute the reflection, transmission, and absorption coefficients following the method explained in Sect. 3.4 of Soler et al. (2019). The time-averaged energy flux is decomposed into its parallel (upward) and antiparallel (downward) components as $\langle\mathbf{\Pi}\rangle = \langle\mathbf{\Pi}\rangle^{\uparrow} - \langle\mathbf{\Pi}\rangle^{\downarrow}$, with

$$\langle\mathbf{\Pi}\rangle^{\uparrow} = \frac{1}{8}\sqrt{\frac{\rho}{\mu}}Z^{\uparrow}Z^{\uparrow *}\,\mathbf{B}, \tag{27}$$

$$\langle\mathbf{\Pi}\rangle^{\downarrow} = \frac{1}{8}\sqrt{\frac{\rho}{\mu}}Z^{\downarrow}Z^{\downarrow *}\,\mathbf{B}, \tag{28}$$

where $\langle\mathbf{\Pi}\rangle^{\uparrow}$ and $\langle\mathbf{\Pi}\rangle^{\downarrow}$ correspond to the time-averaged energy fluxes associated with the upward propagating and downward propagating Alfvén waves, respectively, with $Z^{\uparrow}$ and $Z^{\downarrow}$ the Elsässer variables defined as

$$Z^{\uparrow} = v'_{\varphi} - \frac{1}{\sqrt{\mu\rho}}B'_{\varphi}, \tag{29}$$

$$Z^{\downarrow} = v'_{\varphi} + \frac{1}{\sqrt{\mu\rho}}B'_{\varphi}. \tag{30}$$

We averaged $\langle\mathbf{\Pi}\rangle^{\uparrow}$ and $\langle\mathbf{\Pi}\rangle^{\downarrow}$ horizontally using Eq. (26). Then, the relative values of the vertical components of $\langle\mathbf{\Pi}\rangle^{\uparrow}_{\text{av.}}$ and $\langle\mathbf{\Pi}\rangle^{\downarrow}_{\text{av.}}$ at the photospheric and coronal boundaries indicate the fractions of the injected wave energy that are reflected back to the photosphere, transmitted to the corona, or dissipated in between. Therefore, we defined the reflection, $\mathcal{R}$, transmission, $\mathcal{T}$, and absorption, $\mathcal{A}$, coefficients as

$$\mathcal{R} = \frac{\langle\mathbf{\Pi}\rangle^{\downarrow}_{\text{av.}}\big|_{\text{photosphere}}\cdot\hat{e}_z}{\langle\mathbf{\Pi}\rangle^{\uparrow}_{\text{av.}}\big|_{\text{photosphere}}\cdot\hat{e}_z}, \tag{31}$$

$$\mathcal{T} = \frac{\langle\mathbf{\Pi}\rangle^{\uparrow}_{\text{av.}}\big|_{\text{corona}}\cdot\hat{e}_z}{\langle\mathbf{\Pi}\rangle^{\uparrow}_{\text{av.}}\big|_{\text{photosphere}}\cdot\hat{e}_z}, \tag{32}$$

$$\mathcal{A} = 1 - \mathcal{R} - \mathcal{T}, \tag{33}$$

where the absorption coefficient is simply computed by invoking conservation of energy.

Figure 5 displays, on a logarithmic scale, the three coefficients as functions of the driven wave frequency for the two models. The absorption is barely distinguishable between the models and is therefore not discussed further. The transmissivity curves in the two models are also almost identical, but a small difference is appreciable at frequencies around 5 mHz. To better highlight this small discrepancy, Fig. 6 shows both transmissivity curves again, but using a linear scale on the vertical axis. As discussed in Soler et al. (2019) and Morton & Soler (2025), the shape of the transmission curve can be approximated by a skewed log-normal function, with a steep tail toward high frequencies and a gentler tail toward low frequencies. This shape is reproduced well by both models, although a discrepancy between them is noticeable around the maximum of the curve, where the single-fluid model yields a slightly larger transmissivity.

Going back to Fig. 5, the most relevant difference between the models appears in the reflectivity at frequencies exceeding

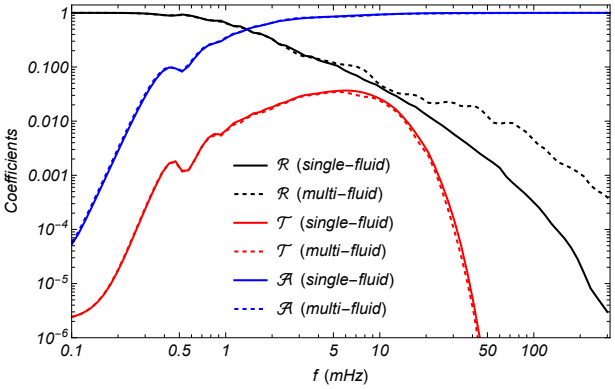

Fig. 5. Coefficients of reflectivity, $\mathcal{R}$, transmissivity, $\mathcal{T}$, and absorption, $\mathcal{A}$, as functions of the wave frequency in the single-fluid and multi-fluid models. Note that both axes are in log-scale.

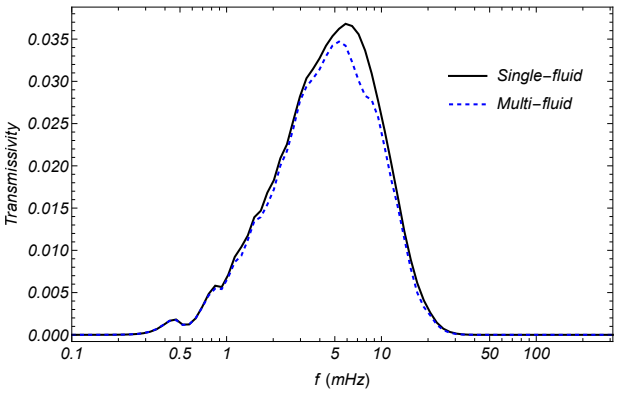

Fig. 6. Transmission coefficient as a function of the wave frequency in the single-fluid and multi-fluid models. Note that the frequency axis is in log-scale.

approximately 10 mHz. Above this frequency, the reflectivity in the single-fluid model decreases more rapidly with frequency than in the multi-fluid model. The reflection of Alfvén waves depends on the relationship between the wavelength and the scale height associated with the gradients of density and magnetic field strength (see, e.g., Ferraro 1954). In the single-fluid model, the relevant density is the total (ion plus neutral) density, since all species are assumed to be strongly coupled regardless of the wave frequency. Conversely, in the multi-fluid model, the effective density felt by the Alfvén waves depends on the frequency (see Eq. (34) of Soler et al. 2019), because the ion–neutral coupling weakens as the frequency increases. Therefore, the density gradient experienced by the Alfvén waves becomes progressively different in the single-fluid and multi-fluid models as the frequency increases, becoming slightly steeper in the multi-fluid model. This results in a lower reflectivity in the single-fluid model. In summary, the combined effect of the slightly larger transmissivity around the 5 mHz peak and, more importantly, the lower reflectivity at frequencies higher than 10 mHz can explain why the energy transmitted to the corona is slightly larger in the single-fluid model.

Finally, we examined the differences in the heating rate associated with the dissipation of wave energy. As in the case of the energy flux, we considered the horizontally averaged heating rate computed using an expression equivalent to Eq. (26). The top panel of Fig. 7 shows the averaged total heating rate as a function of height above the photosphere. Once again, it is

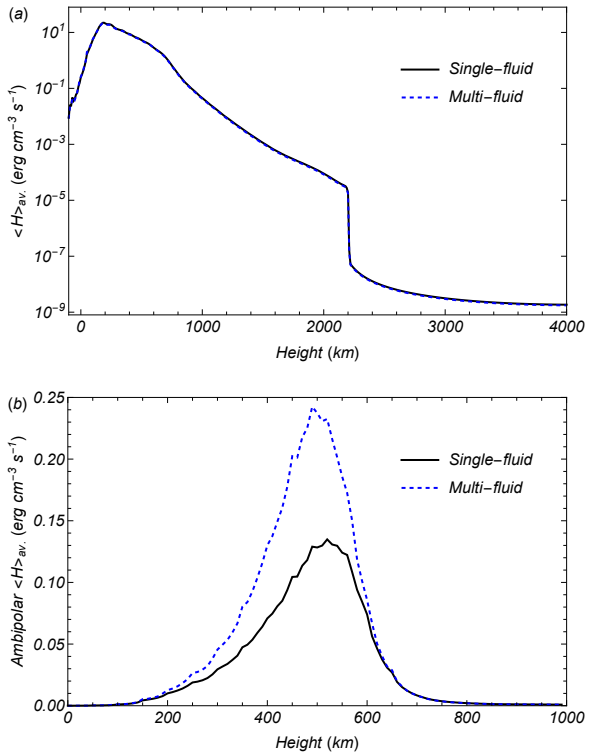

Fig. 7. Dependence on height above the photosphere of the horizontally averaged total heating rate (top) and ambipolar heating rate (bottom) in the single-fluid and multi-fluid cases. Note that the bottom panel only displays heights below 1000 km.

remarkable how similar the results are for the two models, which appear nearly superimposed in the figure. According to Eq. (25), the total heating rate is the sum of the Ohmic and ambipolar contributions, with frictional heating replacing ambipolar heating in the multi-fluid description (see Eq. (58) of Soler et al. 2019). We compared these contributions separately for both models. The Ohmic heating is, once more, nearly identical in the two models, and its comparison is not shown here for the sake of simplicity. The ambipolar and frictional heating rates are also extremely similar at all heights, with the exception of a narrow region around 500 km above the photosphere. The bottom panel of Fig. 7 compares the ambipolar and frictional heating rates of the two models in the vicinity of this region, where it can be seen that the single-fluid model underestimates the heating rate by approximately a factor of two compared with the multi-fluid result. The reason for this discrepancy lies in the approximate description of the ion-neutral drifts in the single-fluid model. For the multi-fluid model, Fig. 7a of Soler et al. (2019) shows the averaged ion-neutral drift as a function of height at three different radial positions in the flux tube. The height at which these drifts attain their largest values in the chromosphere coincides with the region of discrepancy discussed here. This height also corresponds to the location in the atmosphere where the neutral-ion collision frequencies reach their minimum (see again Fig. 2). This clearly indicates that the drifts are only partially captured by the single-fluid approximation, which leads to an underestimation of the associated heating rate in the single-fluid model.

4. Discussion

The purpose of this paper has been to compare the results of multi-fluid and single-fluid models for the propagation of

torsional Alfvén waves from the photosphere to the corona along a vertical magnetic flux tube that expands with height. The results of the multi-fluid model were obtained in Soler et al. (2019). Overall, the differences between the two models are negligible, with only two noticeable discrepancies. First, the single-fluid model allows slightly more wave energy (about 5% more) to reach the corona than the multi-fluid model. This difference is explained by the lower reflectivity at high frequencies and the slightly higher transmissivity around the 5 mHz peak obtained in the single-fluid model. Second, in a layer located around 500 km above the photosphere, the ambipolar heating rate predicted by the single-fluid model is approximately a factor of two lower than the corresponding frictional heating rate in the multi-fluid model. This discrepancy arises from the approximate treatment of ion-neutral drifts in the single-fluid formulation, which become significant at those heights. In summary, for the description of Alfvén waves in the lower solar atmosphere, the single-fluid approximation yields remarkably accurate results when compared with the more physically applicable multi-fluid model.

Recently, Gómez-Míguez et al. (2025) compared single-fluid and multi-fluid results for MHD wave propagation in the lower solar atmosphere; their study and the present paper therefore share a common goal. However, the background configuration, methodology, and type of wave studied differ. Gómez-Míguez et al. (2025) considered fast magneto-acoustic waves in a stratified atmosphere of pure hydrogen with a homogeneous horizontal magnetic field, whereas we studied torsional Alfvén waves in a hydrogen–helium stratified atmosphere with a vertical flux tube that expands with height. They employed weakly nonlinear, time-dependent simulations complemented by analytical approximations based on the eikonal approach, while we numerically solved the linearized equations in the stationary state. Here we considered the effects of Ohm's and ambipolar diffusion, while Gómez-Míguez et al. (2025) only included ambipolar diffusion. Despite these differences, a particular finding of Gómez-Míguez et al. (2025) can be meaningfully compared with our results. Similar to what we find here, Gómez-Míguez et al. (2025) show that fast waves in the multi-fluid model transport less energy upward than in the single-fluid model. They explained this behavior by noting that the multi-fluid model is more efficient at dissipating energy at low heights than the single-fluid model. This result qualitatively agrees with Fig. 7b, although in our case it is not the main mechanism responsible for the reduced Alfvén wave energy transport to the corona in the multi-fluid model. Instead, we attribute this difference to variations in the atmospheric reflectivity that appear at high frequencies, when the effective density felt by the Alfvén waves in the multi-fluid model begins to differ from the total density.

Another difference with the study by Gómez-Míguez et al. (2025) is that the Alfvén waves investigated here are incompressible, whereas fast magneto-acoustic waves are compressible. Consequently, all the effects associated with compressibility, pressure variations, and related phenomena discussed in Gómez-Míguez et al. (2025) are not applicable to the case of Alfvén waves.

Finally, it is worth noting that the main conclusion of this work, namely the excellent accuracy of the single-fluid model, is not generalizable beyond the specific context of the solar atmospheric Alfvén waves studied here. Processes such as shocks and instabilities in partially ionized solar and astrophysical plasmas exhibit distinctive features when investigated with multi-fluid models that cannot be reproduced by the single-fluid approximation (see Soler & Ballester 2022, Hillier & Snow 2023, and references therein). We also note that the highest wave frequency included in our analysis was 300 mHz, and that more significant differences between the models may emerge if higher frequencies are considered (see, e.g., Soler et al. 2013; Martínez-Gómez 2025). However, observations by Matsumoto & Shibata (2010), Matsumoto & Kitai (2010), and Chitta et al. (2012) indicate that the power of horizontal photospheric motions decreases rapidly toward higher frequencies. Therefore, it is unlikely that very high-frequency Alfvén waves are driven in the photosphere with sufficient energy to play a significant role.

Acknowledgements. This publication is part of the R+D+i project PID2023-147708NB-I00, funded by MCIN/AEI/10.13039/501100011033 and by FEDER, EU. The author acknowledges David Martínez-Gómez for a useful discussion and an anonymous referee for a constructive report.

References

Alfvén, H. 1947, MNRAS, 107, 211
Arber, T. D., Brady, C. S., & Shelyag, S. 2016, ApJ, 817, 94
Ballester, J. L., Alexeev, I., Collados, M., et al. 2018, Space Sci. Rev., 214, 58
Cally, P. S. 2023, ApJ, 954, 85
Cally, P. S., & Khomenko, E. 2019, ApJ, 885, 58
Chitta, L. P., van Ballegooijen, A. A., Rouppe van der Voort, L., DeLuca, E. E., & Kariyappa, R. 2012, ApJ, 752, 48
De Pontieu, B., Carlsson, M., Rouppe van der Voort, L. H. M., et al. 2012, ApJ, 752, L12
De Pontieu, B., Rouppe van der Voort, L., McIntosh, S. W., et al. 2014, Science, 346, 1255732
Díaz-Suárez, S., & Soler, R. 2021, A&A, 648, A22
Erdélyi, R., & Fedun, V. 2007, Science, 318, 1572
Ferraro, V. C. A. 1954, ApJ, 119, 393
Fontenla, J. M., Avrett, E. H., & Loeser, R. 1993, ApJ, 406, 319
Forteza, P., Oliver, R., Ballester, J. L., & Khodachenko, M. L. 2007, A&A, 461, 731
Gómez-Míguez, M. M., Martínez-Gómez, D., Khomenko, E., et al. 2025, A&A, 701, A196
Goodman, M. L. 2011, ApJ, 735, 45
Guo, M., Van Doorsselaere, T., Karampelas, K., et al. 2019, ApJ, 870, 55
Hillier, A. S. 2024, Philos. Trans. R. Soc. Lond. Ser. A, 382, 20230229
Hillier, A., & Snow, B. 2023, Adv. Space Res., 71, 1962
Jess, D. B., Mathioudakis, M., Erdélyi, R., et al. 2009, Science, 323, 1582
Khodachenko, M. L., Arber, T. D., Rucker, H. O., & Hanslmeier, A. 2004, A&A, 422, 1073
Khomenko, E., & Collados, M. 2012, ApJ, 747, 87
Khomenko, E., Collados, M., Díaz, A., & Vitas, N. 2014, Phys. Plasmas, 21, 092901
Leake, J. E., Arber, T. D., & Khodachenko, M. L. 2005, A&A, 442, 1091
Maneva, Y. G., Alvarez Laguna, A., Lani, A., & Poedts, S. 2017, ApJ, 836, 197
Martínez-Gómez, D. 2025, ApJ, 982, 4
Martínez-Gómez, D., Soler, R., & Terradas, J. 2017, ApJ, 837, 80
Martínez-Gómez, D., Soler, R., & Terradas, J. 2018, ApJ, 856, 16
Martínez-Sykora, J., De Pontieu, B., Hansteen, V., & Carlsson, M. 2015, Philos. Trans. R. Soc. Lond. Ser. A, 373, 20140268
Matsumoto, T., & Kitai, R. 2010, ApJ, 716, L19
Matsumoto, T., & Shibata, K. 2010, ApJ, 710, 1857
Morton, R. J., & Soler, R. 2025, ApJ, 986, L6
Morton, R. J., Gao, Y., Tajfirouze, E., et al. 2026, Nat. Astron., 10, 42
Pelekhata, M., Murawski, K., & Poedts, S. 2021, A&A, 652, A114
Popescu Braileanu, B., Lukin, V. S., Khomenko, E., & de Vicente, Á. 2019, A&A, 627, A25
Soler, R. 2024, Philos. Trans. R. Soc. Lond. Ser. A, 382, 20230223
Soler, R. 2025, A&A, 702, A16
Soler, R., & Ballester, J. L. 2022, Front. Astron. Space Sci., 9, 789083
Soler, R., Carbonell, M., Ballester, J. L., & Terradas, J. 2013, ApJ, 767, 171
Soler, R., Terradas, J., Oliver, R., & Ballester, J. L. 2017, ApJ, 840, 20
Soler, R., Terradas, J., Oliver, R., & Ballester, J. L. 2019, ApJ, 871, 3
Song, P., & Vasyliūnas, V. M. 2011, J. Geophys. Res.: Space Phys., 116, A09104
Tu, J., & Song, P. 2013, ApJ, 777, 53
Walker, A. D. M. 2005, Magnetohydrodynamic Waves in Geospace (Institute of Physics Publishing)
Zaqarashvili, T. V., Khodachenko, M. L., & Rucker, H. O. 2011, A&A, 529, A82
Zaqarashvili, T. V., Khodachenko, M. L., & Soler, R. 2013, A&A, 549, A113